POLYOXOMETALATES

Open Access
RESEARCH ARTICLE

Synergistic polyoxometalate–bimetal oxide in hierarchical porous nanofibers for high-rate, long-life lithium-ion anodes

Yangyang Liu[1,2,§], Yuwen Wang[1,2,§], Li Sun[3], Pengyu Zhu[1], Liping Cui[1,2] ✉, Ziyue Han[1,2], and Kai Yu[1,2] ✉

[1] *School of chemistry and chemical engineering, Harbin Normal University, Key Laboratory for Photonic and Electronic Bandgap Materials, Ministry of Education, Harbin 150025, China*
[2] *Key Laboratory of Photochemical Biomaterials and Energy Storage Material, Heilongjiang Province, Harbin Normal University, Harbin 150025, China*
[3] *Heilongjiang Province Key Laboratory of Geographical Environment Monitoring and Spatial Information Service in Cold Regions, Harbin Normal University, Harbin 150025, China*
[§] *Yangyang Liu and Yuwen Wang contributed equally to this work.*

Cite This: *Polyoxometalates*, **2026**, *5*, 9140135

Read Online

ABSTRACT: The integration of functionally complementary materials into a unified architecture is an effective strategy for the development of advanced electrodes. Therefore, this study synthesized a hierarchical porous carbon nanofiber composite (PWN/$FeVO_4$@CNF) that incorporates Ni-substituted Keggin-type phosphotungstate (PWN) and bimetal oxide $FeVO_4$ via electrospinning and controlled calcination. As an anode for lithium-ion batteries (LIBs), PWN/$FeVO_4$@CNF outperforms its individual components, thereby achieving a high discharge capacity of 1327.7 mA·h·g^{-1} at 0.1 A·g^{-1}. Additionally, it exhibits exceptional durability, retaining a capacity of 1280.0 mA·h·g^{-1} after 500 cycles, and maintains 715.4 mA·h·g^{-1} at a high current density of 2 A·g^{-1}. These properties are derived from an enhanced Li^+ diffusion coefficient, reduced charge-transfer resistance, and an enlarged electrochemical surface. Kinetic analyses reveal a hybrid storage mechanism involving diffusion-controlled ($i \propto v^{1/2}$) and pseudocapacitive ($i \propto v$) processes, with the latter dominating at higher scan rates. The synergistic combination of PWN's multielectron redox activity and $FeVO_4$'s high capacity, within a conductive and buffering carbon matrix, leads to outstanding LIB performance. This approach effectively addresses the poor conductivity and severe volume expansion associated with individual metal oxides while maximizing their high-capacity advantages.

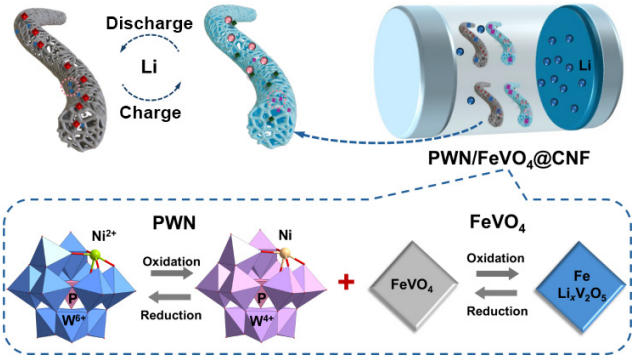

KEYWORDS: lithium ion battery, Keggin-type polyoxometalates, bimetallic oxides, composite nanofibers, hierarchical porous structure

1 Introduction

Lithium-ion batteries (LIBs) have emerged as vital energy storage technology, powering diverse applications from electric vehicles to portable electronics, due to their excellent energy density (250–300 Wh·kg^{-1}), prolongated circulationcycle stability (> 1000 cycles), and minimal self-discharge (< 5% per month) [1–4]. Owing to the dual challenges of environmental sustainability and fossil fuel depletion, ongoing research is driven toward eco-friendly, high-efficiency storage solutions [5]. Currently, commercial LIBs primarily use graphite as the anode material because of its excellent electrochemical stability and cost-effectiveness [6]. However, graphite's limited theoretical capacity (372 mA·h·g^{-1}) and inferior rate capability hinder its application in next-generation high-energy-density battery systems. Conversely, Si-based materials offer high capacity but suffer from severe volume expansion and poor cycle stability [7]. Additionally, transition metal [8, 9] and alloy-type materials [10] encounter challenges such as low conductivity and structural degradation. Therefore, multicomponent composites that synergistically integrate the advantages of each constituent are essential to overcome these tradeoffs and satisfy the increasing performance demands of advanced energy storage devices.

Polyoxometalates (POMs) possess unique physicochemical properties, including tunable surface charge, high thermal stability, and extensive multielectron redox activity. Through compared to conventional materials, structural modifications have led to considerable performance enhancements [11]. In addition, their open quasimolecular framework facilitates unobstructed lithium-

Received: March 16, 2026; **Revised:** April 14, 2026
Accepted: May 7, 2026

✉Address correspondence to Liping Cui, hsdclp1995@hrbnu.edu.cn; Kai Yu, yukai@hrbnu.edu.cn

https://doi.org/10.26599/POM.2026.9140135

ion transport between surfaces and clusters, positioning POMs as ideal candidates for next-generation batteries. However, their practical application in energy storage is hindered by inherent limitations, including low intrinsic electronic conductivity and restricted accessible surface area [12, 13]. These limitations can be effectively addressed with the uniform dispersion of POMs as molecularly thin layers on nanostructured scaffolds that maximize exposure to redox centers or by anchoring them to conductive networks that connect each cluster to the current collector [14]. Representative systems, such as $MnPMo_8V_6$@MXene/MoS_2 [15], $NiCo_2S_4$/PANI@POM/rGO [16], $CoNiO_2$@NiP_6Mo_{18}/CNTs [17], PVW@CoATP [18], and CuP_6Mo_{18}@/ZnO/CNFs [19] have demonstrated that integrating POMs with carbon-based materials and/or nanometal oxides substantially enhances LIB performance. This improvement originates from optimized ion-transport pathways, increased electrochemically active surface areas, and the introduction of additional mobile charge-carrier sites. Collectively, these synergistic effects facilitate fast charge transfer and efficient utilization of the active material, resulting in superior overall electrochemical performance [20, 21]. Building on these findings, the study aims to select an optimal precursor and develop a composite-based anode material for a LIB anode that delivers balanced and outstanding performance.

Bimetallic oxides are promising LIB anode candidates due to their high theoretical capacity, abundant redox-active sites, and tunable chemical compositions. However, traditional bimetallic oxides suffer from severe volume expansion, poor conductivity, and structural degradation during cycling, which limit their practical use in LIBs [22–25]. By contrast, hollow and surface-porous bimetallic oxide nanofibers effectively overcome these drawbacks by providing sufficient internal void space to accommodate volume changes, reducing ion diffusion pathways, and enhancing structural integrity, thereby minimizing electrode pulverization and capacity loss [26–28]. Recently, V-based hollow bimetallic oxide nanofibers have gained attention as LIB anodes [29–33]. These materials not only retain the intrinsic properties of V-based compounds but also leverage their tubular morphology to enhance electron transport, facilitate high ion flux, and ultimately improve energy storage performance, cycling stability, and rate capability. Electrospinning technology allows for the customizable fabrication of diverse metal oxide nanofibers and integration of multiple materials and architectures, thereby enabling the design of high-performance nanofiber composites with tailored properties. By harnessing the flexibility of electrospinning, V-based bimetallic oxides, Keggin-type POMs, and carbon materials can be effectively combined into hollow, porous, and multifunctional nanofibers. This design exploits the synergistic interactions among complementary components and the benefits of heterostructure systems, collectively enhancing capacity, conductivity, stability, and rate capability in LIBs [34].

Based on these preceding insights, a composite nanofiber with a multilevel pore structure, referred to as PWN/$FeVO_4$@CNF, was designed and synthesized through electrospinning, followed by carefully regulated calcination. This composite synergistically combines the advantages of POMs, bimetallic oxides, and porous carbon nanofibers. As an anode for LIBs, it exhibits notable enhancements in specific capacity, electrical conductivity, long-term cycling stability, and rate capability. These advantages originate from its structural features: The uniform dispersion of POMs and $FeVO_4$ within the porous one-dimensional (1D) scaffold optimally utilizes their redox-active sites, whereas the multiscale porous network facilitates efficient electron transfer and rapid lithium-ion transport.

2 Experimental

2.1 Material synthesis

2.1.1 Synthesis of $Na_5PW_{11}NiO_{39}{\cdot}nH_2O$ (PWN)

Based on the improved method detailed in Ref. [35], the specific preparation methods are as follows. A 0.5-M sodium bicarbonate ($NaHCO_3$) solution was synthesized by dissolving 4.2005 g of $NaHCO_3$ in deionized water. This solution was added dropwise to a mixture of 0.2 mmol phosphotungstic heteropoly acid ($H_3PW_{12}O_{40}{\cdot}xH_2O$) and nickel sulfate ($NiSO_4$) at a 1:1 ratio until the pH reached 5. The mixture was then heated in a bain-marie at 60 °C for 5 h. After evaporation to saturation, the solution was allowed to cool and crystallize, resulting in the formation of needle-like $NaHCO_3$ crystals, which were filtered out to yield the final bulk product, $Na_5PW_{11}NiO_{39}$ phosphotungstate (PWN).

2.1.2 Synthesis of porous nanofibers ($FeVO_4$@CNF)

A solution was prepared by dissolving 0.3535 g of iron(III) acetylacetonate ($C_{15}H_{21}FeO_6$, 98%) and 0.2655 g of vanadium(III) acetylacetonate ($C_{15}H_{21}VO_6$, 97%) in 2.5 g of N,N-dimethylformamide (DMF). Following stirring at 25 °C for 10 min, 0.5 g of polyvinylpyrrolidone (PVP, M_W = 130,000) was added, and the mixture was stirred for an additional 80 m. Subsequently, the resulting solution was transferred into a 5 mL disposable medical syringe. An electric field voltage of 12 kV was applied, with a distance of 15 cm between the syringe nozzle and the Al plate. The precursor solution was spun directly onto the aluminum plate to form FeV-PVP precursor nanofibers. These nanofibers were subsequently calcined in air at a heating rate of 2 °C·min^{-1} for 3 h at temperatures of 400, 500, and 600 °C, yielding nanofibers designated as 400-$FeVO_4$@CNF, 500-$FeVO_4$@CNF, and 600-$FeVO_4$@CNF, respectively.

2.1.3 Synthesis of porous nanofibers (PWN/$FeVO_4$@CNF)

$Na_5PW_{11}NiO_{39}$ PWN (0.20 g) was dissolved in 3.00 g of DMF under mixing for 20 min. Next, vanadium(III) acetylacetonate (0.26 g) and iron(III) acetylacetonate (0.35 g) were added, followed by stirring for an additional 20 min. Then, 0.5 g of PVP (M_W = 130,000) was introduced and stirred for 70 min. The resulting solution was subjected to electrospinning at 12 kV to obtain composite precursor fibers, which were then sintered in air at 500 °C for 3 h at an increasing rate of 2 °C·min^{-1}. Figure 1 illustrates the experimental procedure

2.2 Electrochemical measurements

Electrochemical evaluations of the materials and composites were performed using techniques such as electrochemical impedance spectroscopy (EIS), cyclic voltammetry (CV), and galvanostatic charge–discharge (GCD) cycling. The Blue Battery Test System was utilized to perform GCD tests at various current densities, ranging from 0.005 to 3.0 V vs. Li/Li$^+$. EIS testing was conducted under an alternating current voltage margin of 5 mV with a rate sweep from 100 kHz to 0.01 Hz. Cyclic voltammetry (CV) tests were performed with a CHI660 electrochemical station over a voltage range of

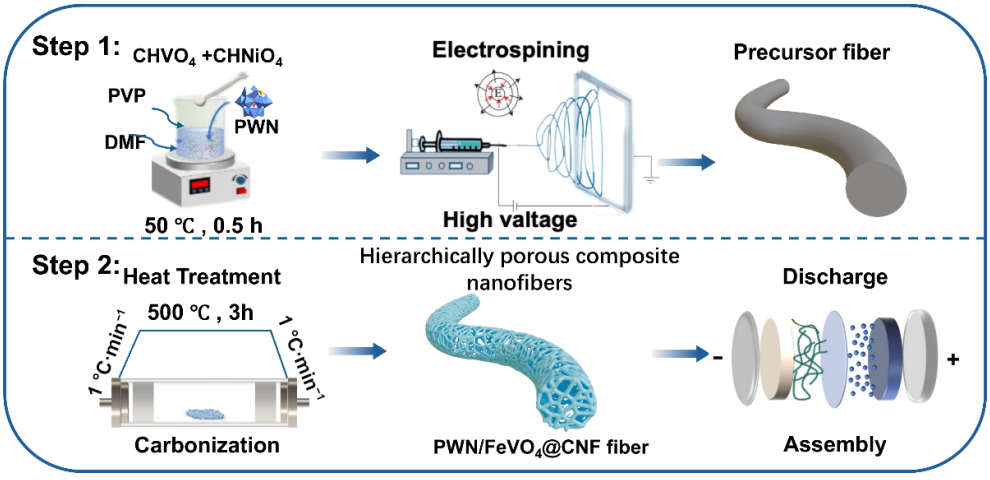

Figure 1 Preparation process diagram of PWN/$FeVO_4$@CNF anode composite material.

0.005–3.0 V vs. Li/Li^+ at different scan rates. In addition, the non-Faradaic bilayer capacitance (C_{dl}) of the composite was determined by analyzing CV curves at multiple scan rates (0.2, 0.4, 0.6, 0.8, and 1.0 $mV{\cdot}s^{-1}$). The electrochemical active surface area (ECSA) of the composite anode material was calculated based on the obtained C_{dl} values. Furthermore, galvanostatic charge discharge (GCD) and galvanostatic intermittent titration technique (GITT) techniques were evaluated using the Blue Battery system in a voltage range of 0.01 to 3.0 V.

2.3 Preparation of electrodes

The anodes were fabricated to assess the electrochemical performance of the batteries. The anode materials, including 400-$FeVO_4$@CNF, 500-$FeVO_4$@CNF, 600-$FeVO_4$, PWN/$FeVO_4$@CNF, and PWN, were combined with lithium acetylene black and polyvinylidene fluoride at a weight ratio of 7:2:1. These mixtures were thoroughly ground, and an appropriate amount of N-methylpyrrolidone was added before grinding again to form a uniform, smooth paste. Subsequently, this paste was applied to copper foil and dried for 10 h at 60 °C under vacuum. Following drying, the copper foil was cut into round tablets with radii of 6 mm which were then pressed at 6 kPa for 15 s to form electrodes. The button batteries were assembled in a glove box under an argon atmosphere. Lithium sheets served as the counter electrodes, and Celgard-2400 membranes with radii of 8 mm were used as separators. The electrolyte solution consisted of 1 M $LiPF_6$ in a 1:1 mixture of ethylene carbonate and dimethyl carbonate, contributing to the batteries' excellent performance.

3 Results and discussion

3.1 Discussion on calcination temperature

To determine the optimal calcination temperature, $FeVO_4$@CNF composites were synthesized at 400, 500, and 600 °C. Scanning electron microscopy (SEM) images (Figs. S1(a)–S1(c) in the Electronic Supplementary Material (ESM)) trace a clear morphological evolution: Fibers produced at 400 °C are dense and nonporous, whereas those at 500 and 600 °C yield hollow tubes with nanoporous walls. Energy dispersive X-ray spectroscopy (EDS) analysis (Figs. S1(d)–S1(f) in the ESM) showed a progressive reduction in carbon content as temperature increased, with the 600 °C sample exhibiting the lowest carbon levels due to extensive decomposition of organic components. Electrochemical screening (Figs. S2(a)–S2(d) in the ESM) identified the 500 °C sample as the top performer, demonstrating the highest CV-integrated charge, the longest galvanostatic discharge plateau, the lowest charge-transfer resistance (R_{ct}), and the smallest Warburg impedance (Z_w). Although its Li^+ diffusion coefficient was slightly lower than that of the 600 °C sample, the overall balance between kinetics and capacity was optimal at 500 °C. Additionally, Fourier transform infrared (FTIR) spectroscopy analysis of PWN revealed that the Keggin structure (characteristic bands at 1100–500 cm^{-1}) remains intact at 400 and 500 °C but collapses at 600 °C (Fig. S3 in the ESM). Therefore, 500 °C was established as the preferred calcination temperature, effectively balancing the preservation of the POM structure with the optimization of electrochemical properties. For clarity in subsequent discussions, the 500-$FeVO_4$@CNF sample is hereafter referred to as $FeVO_4$@CNF.

3.2 Characterization

SEM imaging shows that $FeVO_4$@CNF consists of uniform, 1D hollow tubes with a diameter of 270 nm and textured nanoporous walls (Figs. S4(a)–S4(c) in the ESM). Elemental mapping reveals that Fe, V, O, and C are evenly distributed along the fiber length (Figs. S4(d)–S4(h) in the ESM). Following Keggin-PWN incorporation, the 1D architecture was maintained, but the fiber diameter was reduced to approximately 200 nm, the wall thickened, and the surface became noticeably rougher with well-defined primary particles. Furthermore, TEM characterization clarified the hierarchical porous architecture, showing uniformly distributed pores on the surface and within the nanotube walls, which collectively exhibit a distinctive lotus-root-like cross-sectional morphology (Figs. 2(a)–2(d)). This unique porous tubular configuration enhances Li^+ diffusion kinetics and provides a high specific surface area. The incorporation of Keggin-type POMs induces further surface texturing and modifies the particulate morphology. EDS mapping confirms that Na, Ni, P, W, and additional Fe/V are uniformly codistributed with the original framework elements (Figs. 2(e)–2(i)), demonstrating that PWN clusters are integrated throughout the $FeVO_4$ matrix without any phase segregation. The electrospinning and annealing techniques employed in this study should be readily applicable to other bimetallic oxides and POMs, offering a versatile approach to hierarchically porous, hybrid nanofiber electrodes.

The infrared spectrum of PWN shows five characteristic

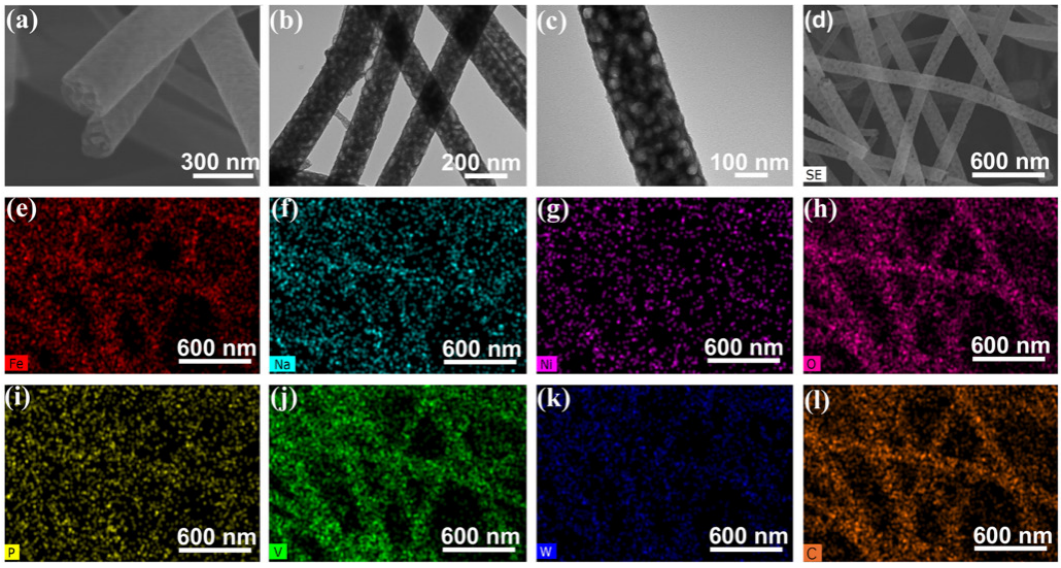

Figure 2 Surface topography of PWN/$FeVO_4$@CNF: (a) SEM image; (b) and (c) TEM images; (d) SEM image; EDS mappings of (e) Fe, (f) Na, (g) Ni, (h) O, (i) P, (j) V, (k) W, (l) C.

absorption bands in the Keggin-structure fingerprint region (Fig. 3(a)), which correspond to the following fundamental vibrations: 1084 cm^{-1} (asymmetric P–O stretching), 1054 cm^{-1} (terminal W=O bonds), and three bridging-oxygen signatures at 967, 899, and 813 cm^{-1}. These spectral features align well with the reported vibrational signatures of the $Na_5PW_{11}NiO_{39}$ Keggin structure [36]. In the composite spectrum, all five PWN signatures are preserved, whereas additional peaks from $FeVO_4$ and the carbon scaffold are clearly resolved [37], confirming that the Keggin cluster remains structurally intact during the electrospinning and annealing process. X-ray diffraction (XRD) analysis confirmed the crystalline structure of the as-synthesized $FeVO_4$ nanofibers (Fig. 3b). All major diffraction peaks correspond closely with the standard $FeVO_4$ pattern (JCPDS 71-1592), indicating successful formation of the target phase. The XRD pattern of the composite retains all characteristic peaks of PWN and $FeVO_4$/C, confirming the effective integration of these components within the PWN/$FeVO_4$@C hybrid material.

X-ray photoelectron spectroscopy (XPS) was used to analyze the elemental composition and oxidation states of PWN/$FeVO_4$@CNF. The survey spectrum (Fig. 3(c)) confirmed the presence of Na, Fe, Ni, V, O, P, W, and C. In the high-resolution Fe 2p spectra (Fig. 3(d)), the spin-orbit splitting between the $2p_{3/2}$ and $2p_{1/2}$ peaks was measured at approximately 13.95 eV, indicating the presence of Fe^{3+}. The spectrum was deconvoluted into four components: two corresponding to Fe^{2+} with binding energies of 711.20 eV ($2p_{3/2}$) and 725.20 eV ($2p_{1/2}$), and two corresponding to Fe^{3+} at 713.70 eV ($2p_{3/2}$) and 728.01 eV ($2p_{1/2}$). A peak at 708.75 eV indicated a small amount of surface Fe resulting from Fe^{3+}/Fe^{2+} reduction. Satellite peaks, attributed to multiplet splitting or energy loss processes, appeared on the high-binding-energy side of the two main Fe^{3+} signals [38, 39]. In the V 2p spectrum (Fig. 3(e)), the spin-orbit splitting between the $2p_{3/2}$ and $2p_{1/2}$ peaks was found to be 7.68 eV, characteristic of the V^{5+} oxidation state. The fitted spectrum revealed two doublets: The first pair at 516.90 eV ($2p_{3/2}$) and 523.70 eV ($2p_{1/2}$) was assigned to V^{4+}, and the second pair at 517.70 eV ($2p_{3/2}$) and 525.30 eV ($2p_{1/2}$) corresponded to V^{5+} [38]. In the Ni 2p spectrum (Fig. 3(f)), peaks for Ni^{2+} were observed at 855.60 eV ($2p_{3/2}$) and 873.50 eV ($2p_{1/2}$), along with two associated satellite features [40–42]. The W 4f spectrum (Fig. 3(g)) of W^{6+} displayed a doublet at 35.97 eV ($4f_{7/2}$) and 38.09 eV ($4f_{5/2}$) [43]. The C 1s spectrum (Fig. 3(h)) was deconvoluted into four components: C–C/C=C (284.80 eV), C–N (286.20 eV), C–O (288.30 eV), and a satellite peak at 289.29 eV [44]. The O 1s spectrum (Fig. 3(i)) was fitted into three components at 530.40, 531.80, and 533.00 eV, corresponding to W/V–O bonds, Fe–O bonds, and oxygen vacancies, respectively [45]. The coexistence of oxygen vacancies, V^{4+}/V^{5+}, and Fe^{2+}/Fe^{3+} suggests a rich presence of cationic defects, which collectively enhance the electron-hopping mechanism, improving electronic and ionic conductivity in the composite. These defect features effectively modulate the electronic structure of the composite, making it a promising semiconductor and potential anode material for LIBs [46, 47]. N_2 adsorption–desorption measurements indicate that both porous materials exhibited microporous and mesoporous characteristics with an H3-type hysteresis loop (Fig. S5 in the ESM). Specifically, $FeVO_4$@CNF shows a bimodal pore-size distribution with average pore widths of 0.602 nm (micropores) and 8.87 nm (mesopores), corresponding to a Brunauer–Emmett–Teller (BET) surface area of 270.46 $m^2 \cdot g^{-1}$. In comparison, PWN/$FeVO_4$@CNF featured an interconnected, lotus root-like pore network that broadened the average mesopore size to 12.98 nm and increases the BET surface area to 300.32 $m^2 \cdot g^{-1}$. This hierarchical porous architecture is advantageous for accelerating Li^+ transport kinetics and improving the electrochemical properties of the composites.

3.3 Electrochemical properties of PWN/$FeVO_4$@CNF

The electrochemical performance of PWN/$FeVO_4$@CNF, along with control samples, $FeVO_4$@CNF and pure PWN, was assessed using coin cells configured as LIB anodes. Initial characterization involved three consecutive CV cycles at a scan rate of 0.1 $mV \cdot s^{-1}$ within a voltage range of 0.005–3.00 V. The first cathodic scan of PWN/$FeVO_4$@CNF (Fig. 4(a)) displayed reduction peaks at 1.35 V and a broad peak between 0.73 and 0.36 V. These peaks correspond to the conversion of $FeVO_4$ into $Li_xV_2O_5$ and the reduction of Fe^{3+} to Fe^0, represented by $xLi^+ + xe^- + FeVO_4 \rightarrow Fe + Li_xV_2O_5$) [48]. This process is accompanied by the reduction of Ni^{2+} to Ni^0 and the multielectron reduction of tungsten (W^{6+}/W^{5+}/W^{4+}) [49]. In

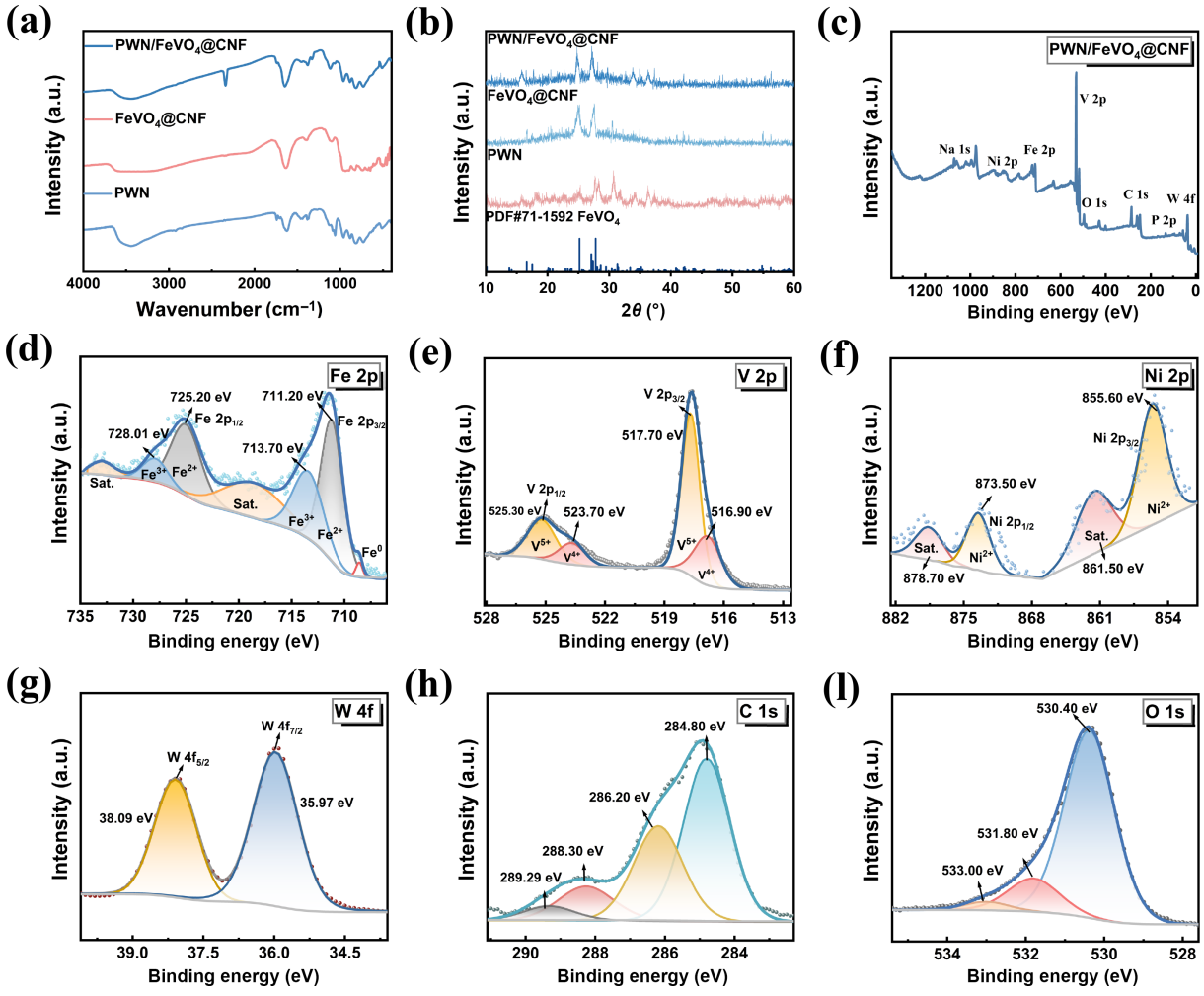

Figure 3 Characterization diagram of PWN, $FeVO_4$@CNF, and PWN/$FeVO_4$@CNF: (a) FTIR spectra; (b) XRD patterns; (c) total XPS spectrum of PWN/$FeVO_4$@CNF; high-resolution XPS spectra of (d) Fe 2p; (e) V 2p; (f) Ni 2p; (g) W 4f; (h) C 1s; (i) O 1s.

addition, the reduction peak at 1.81 V is attributed to the initial reduction of vanadium species (V^{5+}/V^{4+}). In subsequent cycles, the disappearance of the 1.35 V peak indicates an irreversible capacity loss due to the formation of a solid electrolyte interphase (SEI) and electrolyte decomposition during the first cycle [50, 51]. Furthermore, the broad reduction peak (0.73–0.36 V) shifted to 0.75 V in later cycles [52]. The attenuation and shifting of these peaks suggest that irreversible electrochemical reactions occurred during the initial cycle. During the anodic scan, two oxidation peaks were observed at 1.28 and 2.03 V in the first cycle, which shifted to 1.05 and 2.07 V in subsequent cycles. These peaks are associated with the reoxidation of reduced species and lithium extraction from $FeLiV_2O_5$. The nearly overlapping CV curves in later cycles indicate excellent reversibility of lithium-ion intercalation/deintercalation following SEI stabilization. Similar trends were observed in the CV profiles of pure PWN and $FeVO_4$@CNF (Figs. S6(a) and S6(b) in the ESM), where the first cycle exhibited distinct SEI formation features, followed by stable electrochemical behavior in subsequent cycles.

The charge storage mechanisms of the three electrodes were thoroughly examined through kinetic analysis. CV curves were recorded at scan rates ranging from 0.2 to 1.0 $mV \cdot s^{-1}$ (Fig. 4(b) and Fig. S7 in the ESM). Both the PWN@$FeVO_4$/CNF and control samples exhibited quasi-reversible oxidation-reduction peaks, indicating that Faradaic reactions occur at redox-active centers, with pseudocapacitive behavior primarily driving the charge storage process. To quantitatively assess the charge storage behavior, the current response was analyzed using power-law relationships (Eq. (1)) [53]. Linear correlations between logarithmic peak currents ($\lg(i)$) and logarithmic scan rates ($\lg(v)$) were established (Fig. 4(c) and Fig. S8 in the ESM). The derived slope values (b values) provided essential mechanistic insights, with values of 0.911/0.863, 0.848/0.826, and 0.830/0.816 for PWN/$FeVO_4$@CNF, $FeVO_4$@CNF, and PWN, respectively. These intermediate b values ($0.8 < b < 1.0$) confirmed the coexistence of battery-type and pseudocapacitive charge storage mechanisms, consistent with the observed CV characteristics. Further quantitative analysis of the current response distinguished surface-controlled capacitive processes from diffusion-controlled contributions using Eq. (2) [54]. Non-linear fitting analysis was performed to determine the ratios of pseudocapacitive contribution across various scan rates. PWN/$FeVO_4$@CNF showed a progressive increase in pseudocapacitive contributions from 48% to 74% as the scan rate increased from 0.2 to 1.0 $mV \cdot s^{-1}$ (Figs. 4(d) and 4(e), and Fig. S9 in the ESM). Similarly, the pseudocapacitance ratios for $FeVO_4$@CNF and PWN also increased with the scan rate (Figs. S10 and S11 in the ESM). Notably, the composite demonstrated superior pseudocapacitive behavior compared to its individual components,

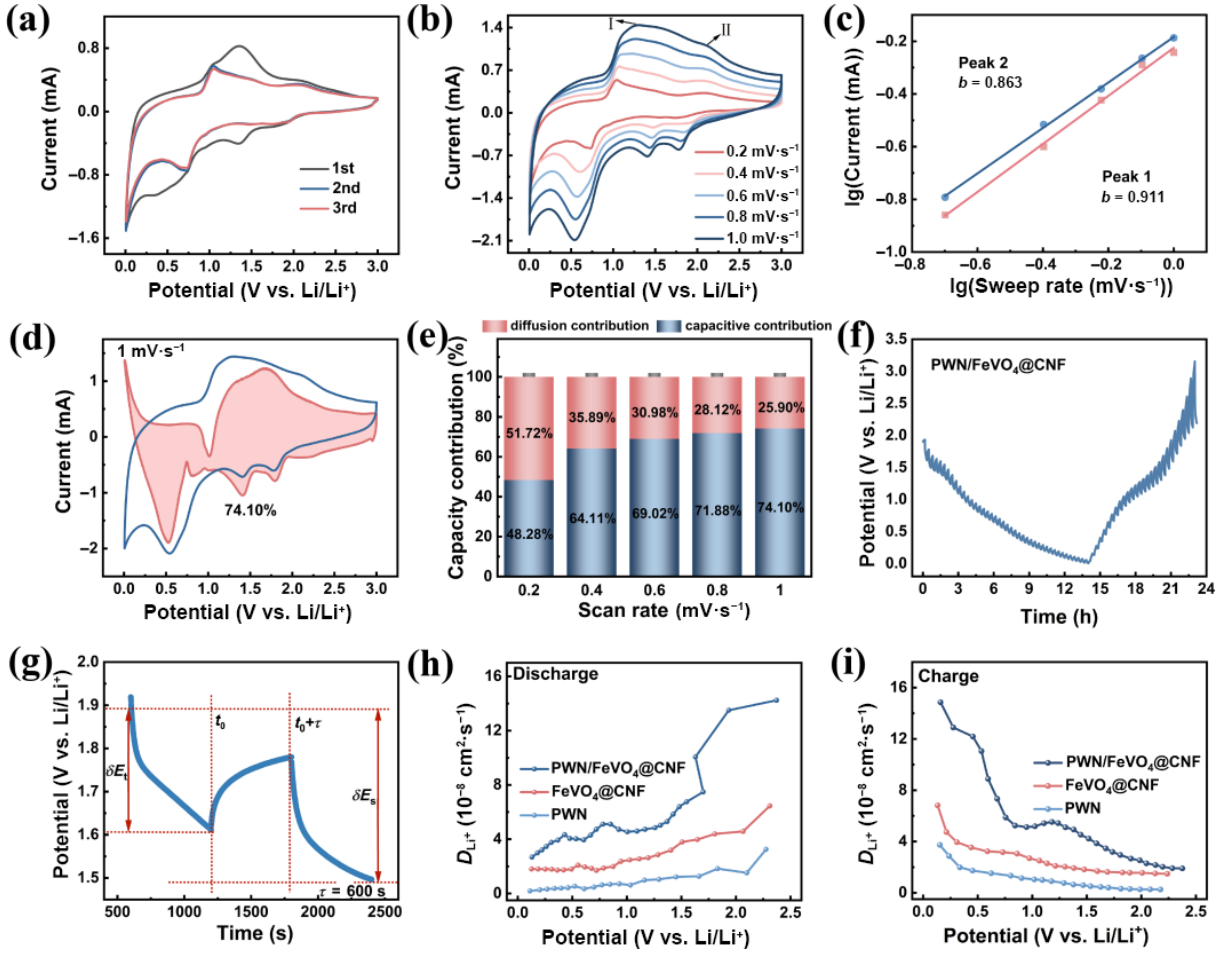

Figure 4 Electrochemical properties of PWN/$FeVO_4$@CNF: (a) initial three CV cycles at 0.1 mV·s^{-1}; (b) CV responses at different scan rates; (c) kinetic analysis of lg(*i*) vs. lg(*v*); (d) capacitive contribution at 1.0 mV·s^{-1}; (e) evolution of charge storage mechanisms with scan rate; (f) GITT measurement at 0.1 A·g^{-1}; (g) single-pulse GITT profile; potential-dependent Li^+ diffusion coefficients during (h) discharge and (i) charge processes, compared with control samples.

as evidenced by its higher *b* values and greater capacitive contribution percentages. This enhancement is attributed to the composite's optimized structure, which offers more redox-active sites and improved charge-transfer kinetics, resulting in enhanced energy storage capabilities.

$$i = av^b \tag{1}$$

$$i(v) = k_1 v + k_2 a v^{1/2} \tag{2}$$

A comparative study of GITT data revealed distinct differences in lithium-ion transport properties among the materials. Figure 4(f) shows the voltage–time profile of PWN/$FeVO_4$@CNF at 0.1 A·g^{-1}, and Fig. 4(g) magnifies a single relaxation–pulse segment to illustrate the transient response. The apparent diffusion coefficient (D_{Li^+}) was calculated using the classical equation [55]

$$D_{Li^+} = \frac{4}{\pi\tau}\left(\frac{m_B V_M}{M_B S}\right)^2 \left(\frac{\Delta E_S}{\Delta E_\tau}\right)^2 \tag{3}$$

The key parameters include the mass of the electrode material (m_B, g), molar volume (V_M, cm^3·mol^{-1}), molar mass (M_B, g·mol^{-1}), surface area of the active material of the electrode (*S*, S·cm^{-2}), duration of the current pulse (τ, s), pulse induced voltage fluctuation (ΔE_S),the constant-current charge and discharge voltage change (iR_{drop}), and the GITT stable voltage shift (ΔE_τ). The GITT curves were analyzed to determine diffusion rates under different potentials. The composite electrode exhibited superior lithium-ion diffusivity, with D_{Li+} values ranging from 1.2088 × 10^{-8} to 1.49974 × 10^{-7} cm^2·s^{-1} during charging and 1.9765 × 10^{-8} to 1.47868 × 10^{-7} cm^2·s^{-1} during discharging, substantially higher than those of the control materials (Table S1 in the ESM, Fig. 4(h) and 4(i)). This enhanced ionic transport is attributed to synergistic structural and compositional advantages: (1) the hierarchical porous architecture derived from the $FeVO_4$/CNF framework, which facilitates rapid Li^+ diffusion, and (2) the incorporation of PWN species, which introduce abundant electroactive sites and promote efficient lithium-ion intercalation/deintercalation. These combined effects contribute to the composite's exceptional electrochemical performance, including improved charge-transfer kinetics and structural stability during cycling [56, 57].

Comprehensive electrochemical characterization was conducted using CV and EIS. Figure 5(a) presents the third-cycle CV profiles of the three electrodes measured at 0.1 mV·s^{-1}. PWN/$FeVO_4$@CNF exhibits the largest area, indicating its superior specific capacity due to the integration of PWN and $FeVO_4$@CNF. This integration increases the number of redox-active sites and facilitates Li^+ insertion and extraction. Nyquist plots (Fig. 5(b)) reveal insights into interfacial charge-transfer characteristics. Each spectrum features a high-frequency intercept, a single compressed semicircle, and an inclined low-frequency tail. The intercept represents the

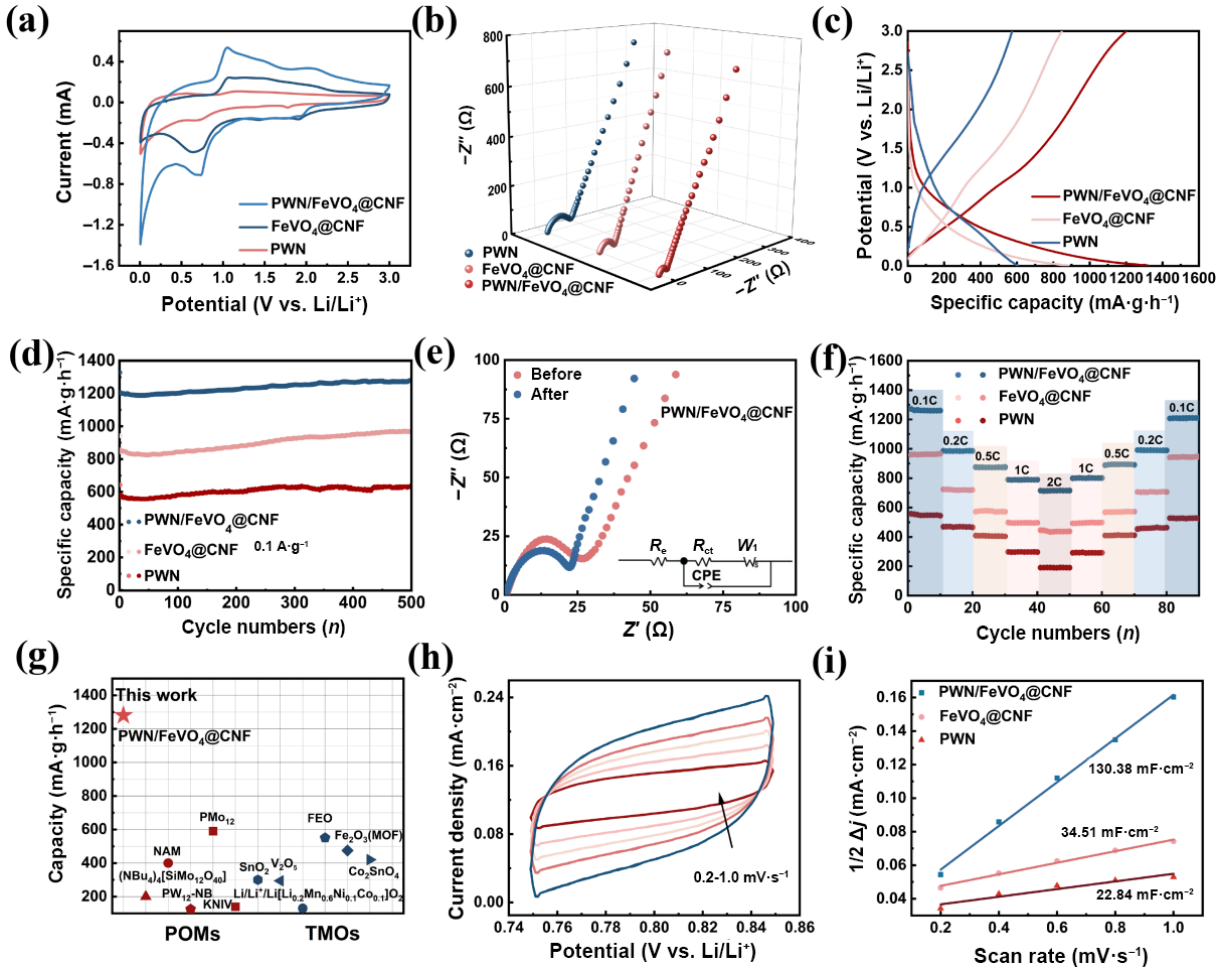

Figure 5 (a) Comparative CV profiles for the initial three cycles of PWN/$FeVO_4$@CNF, $FeVO_4$@CNF, and PWN at 0.1mV·s^{-1}. (b) Nyquist plots and (c) GCD curve at 0.1 A·g^{-1} of three samples. (d) Cycling stability over 500 GCD cycles. (e) Comparative EIS analysis of PWN/$FeVO_4$@CNF before and after cycling. (f) Rate capability at current densities from 0.1 to 2 A·g^{-1}. (g) Ragone plot comparing the capacity of PWN/$FeVO_4$@CNF with other LIB anode materials. (h) CV of PWN/$FeVO_4$@CNF at various scan rates in the non-faradaic potential region. (i) Comparative ECSA analysis of the three samples.

ohmic resistance (R_Ω), the semicircle denotes the combined resistance of the SEI film (R_{SEI}) and charge transfer (R_{ct}), and the tail slope indicates Warburg diffusion impedance (Z_W). The merged semicircle suggests that charge-transfer resistance dominates the electrode kinetics. The composite shows the smallest intercept (1.25 Ω) and arc diameter (27.22 Ω), followed by $FeVO_4$@CNF (1.79, 48.51 Ω) and PWN (2.92, 86.36 Ω), indicating minimized R_Ω and R_{ct} for PWN/$FeVO_4$@CNF. In addition, its steeper low-frequency line corresponds to the lowest Z_W, suggesting rapid ion transport to the electrode interface. This reduction in impedance is attributed to the hierarchical porosity created by the POM–$FeVO_4$ coupling, which shortens Li^+ diffusion paths, and the "electron sponge" behavior of POM, which enhances interfacial charge transfer. Consequently, PWN/$FeVO_4$@CNF achieves reduced overall resistance, improved reaction kinetics, and enhanced electronic conductivity, contributing to its exceptional capacity.

Figure 5(c) compares the GCD profiles of the three electrodes at a current density of 100 mA·g^{-1}. PWN/$FeVO_4$@CNF demonstrates remarkable initial capacities of 1206.0 mA·h·g^{-1} (charge) and 1327.7 mA·h·g^{-1} (discharge), achieving a Coulomb efficiency (CE) of 90.8%. Subsequent cycles show that the GCD curves nearly overlap with CE approaching 100%, confirming excellent electrochemical reversibility and cycling stability, consistent with CV observations (Fig. S12(a) in the ESM). By contrast, the control electrodes show lower initial charge/discharge capacities: $FeVO_4$@CNF (854.9/941.7 mA·h·g^{-1}) and PWN (581.5/642.8 mA·h·g^{-1}), with initial CE values of 90.8% and 90.5%, respectively (Figs. S12(b) and S12(c) in the ESM). The enhanced performance of the composite is attributed to the synergistic integration of $FeVO_4$@CNF with POMs, which creates additional redox-active centers and improves Faradaic charge storage capabilities.

The cycling stability of the PWN/$FeVO_4$@CNF, PWN, and $FeVO_4$@CNF electrodes was evaluated at 0.1 A·g^{-1} (Fig. 5(d)). All three electrodes exhibited a three-phase evolution: an initial capacity drop within the first ~ 50 cycles, a gradual increase between 50 and 350 cycles, and stabilization beyond 350 cycles. The initial decline was primarily attributed to SEI formation, electrolyte depletion, and incomplete electrode wetting. The irreversible capacity loss observed in the first two cycles is characteristic of SEI layer formation. The subsequent capacity increase was due to structural modifications induced by cycling, including the creation of additional active sites and new reactive phases that enhance charge-transfer kinetics. The porous fiber structures of PWN/$FeVO_4$@CNF and $FeVO_4$@CNF facilitated expanded ion pathways and reduced volume changes, with their heterogeneous

interfaces maturing during cycling to promote Li^+ transport. Among these, the hollow $FeVO_4$@CNF demonstrated the most significant recovery due to its highly rearrangeable architecture. During ion insertion and extraction, PWN may disrupt the passivation layer, exposing the internal POM framework, thus allowing more redox centers to participate in the reaction, potentially leading to a gradual increase in capacity. Furthermore, thorough electrolyte wetting may facilitate rapid ion transport, contributing to a rise in capacity. The final stabilized state likely represents an equilibrium condition, where structural activation counterbalances material degradation. After 500 cycles, the specific capacities stabilized at 1280.0, 966.8, and 635.6 $mA{\cdot}h{\cdot}g^{-1}$ for PWN/$FeVO_4$@CNF, $FeVO_4$@CNF, and PWN, respectively. The composite's exceptional cycling stability derives from the synergy of its three components: (1) the porous $FeVO_4$@CNF framework that facilitates ion diffusion, (2) the electron sponge behavior of POM that enables efficient charge transfer, and (3) the carbon substrate that forms a three-dimensional (3D) conductive network. This ternary system enhances conductivity while suppressing capacity fading and structural deformation. Morphological comparison before and after cycling (Fig. S13 in the ESM) revealed that the electrode surface remained intact without noticeable fractures or deformations, further supporting the outstanding structural stability of the composite electrode. Notably, all materials maintained CE values of 99%–100% from the 15th cycle onward (Fig. S14 in the ESM), confirming highly reversible electrochemistry with minimal side reactions [58].

EIS analysis conducted before and after 500 cycles (Fig. 5(e) and Fig. S15 in the ESM) revealed the effects of cycling on interfacial charge-transfer kinetics. Post-cycling, all electrodes exhibited decreased semicircle diameters and increased low-frequency slopes, indicating reduced R_{ct} and Warburg resistance. This evolution is attributed to the progressive electrolyte wetting of the porous nanofiber scaffold and *in situ* formation of a more conductive SEI, which enhances ionic channel width. Notably, $FeVO_4$@CNF exhibited the most significant impedance reduction, likely due to cycling-induced modifications in crystal structure that generated oxygen vacancies and other defects, thereby facilitating charge transfer and ion diffusion. The observed impedance trends align closely with long-term cycling performance. The equivalent circuit model (inset of Fig. 5(e)) encompasses solution resistance (R_e), charge-transfer resistance (R_{ct}), Warburg impedance (W_1), and a constant phase element (CPE1) [56].

Rate capability was evaluated across current density range of 0.1–2 $A{\cdot}g^{-1}$ (Fig. 5(f)). The composite PWN/$FeVO_4$@CNF exhibited reversible capacities of 1250.2, 985.6, 873.5, 789.6, and 715.5 $mA{\cdot}h{\cdot}g^{-1}$ at the respective current densities, significantly outperforming $FeVO_4$@CNF (960.3, 722.4, 569.2, 494.4, and 432.9 $mA{\cdot}h{\cdot}g^{-1}$) and PWN (555.2, 467.0, 407.6, 297.1, and 190.2 $mA{\cdot}h{\cdot}g^{-1}$). At 2 $A{\cdot}g^{-1}$, the composite retained 57.2% of its initial capacity, compared to 45.1% for $FeVO_4$@CNF and 34.3% for PWN, demonstrating exceptional rate capability. When the current density was reverted to 0.1 $A{\cdot}g^{-1}$, the composite recovered to 1210.2 $mA{\cdot}h{\cdot}g^{-1}$, indicating excellent capacity retention and structural reversibility, surpassing both controls (940.5 $mA{\cdot}h{\cdot}g^{-1}$ for $FeVO_4$@CNF and 535.4 $mA{\cdot}h{\cdot}g^{-1}$ for PWN). This impressive performance derives from the synergistic integration within the porous nanofiber architecture: The 3D porous $FeVO_4$@CNF framework promotes rapid Li^+ diffusion, the POM acts as an electron sponge to ensure uniform charge distribution and reduce polarization, and the carbon matrix facilitates continuous electron transport. These characteristics help maintain structural integrity and optimal reaction kinetics under high-rate conditions [59, 60].

Figure 5(g) presents a Ragone plot, showing that PWN/$FeVO_4$@CNF achieved a high reversible capacity of 1280.0 $mA{\cdot}h{\cdot}g^{-1}$ at 0.1 $A{\cdot}g^{-1}$, surpassing many reported LIB anode materials (Table S2 in the ESM). To further investigate the electrochemical energy storage capability, the bilayer capacitance method was employed to estimate the ECSA. CV performed in the nonFaradaic region at various scan rates (Fig. 5(h) and Fig. S16 in the ESM) enabled determination of the double-layer capacitance (C_{dl}) through linear fitting of the charging current (I_c) vs. scan rate (v). The calculated ECSA values (Fig. 5(i)) revealed that PWN/$FeVO_4$@CNF exhibited a substantially higher ECSA (130.38 $mF{\cdot}cm^{-2}$) compared to $FeVO_4$@CNF (34.51 $mF{\cdot}cm^{-2}$) and PWN (22.84 $mF{\cdot}cm^{-2}$). This significant increase in active surface area directly correlates with the composite's superior performance, as enhanced electrode–electrolyte contact facilitates active material participation in redox reactions. The synergistic composite architecture not only increases the electrochemically accessible surface area but also optimizes charge-transfer kinetics, contributing to exceptional capacity and rate capability.

The superior electrochemical performance of PWN/$FeVO_4$@CNF derives from its optimized structural design and synergistic multicomponent interactions. As illustrated in Fig. 6, compared to its individual components, PWN/$FeVO_4$@CNF demonstrates significantly improved lithium-ion transport kinetics. Three key structural features contribute to this enhancement: First, the multiredox activity of PWN, featuring abundant active sites and high thermal stability (maintaining integrity below 500 °C), effectively integrates with the high-surface-area $FeVO_4$@CNF matrix, which is prepared via melt spinning. This combination creates an interconnected network that facilitates rapid ion/electron transfer. Second, the unique honeycomb-briquet architecture shortens ion diffusion paths while maximizing active material–electrolyte contact interfaces, drastically enhancing lithium-ion insertion and extraction kinetics. Third, nitrogen adsorption analyses reveal well-preserved porosity with slightly increased pore size and surface area after 500 cycles, confirming exceptional structural resilience during repeated lithiation/delithiation. This combination effectively mitigates degradation caused by volume changes while maintaining electrochemical activity, thereby accounting for the composite's outstanding cycling stability and rate capability in LIB applications.

4 Conclusions

A composite nanofiber with hierarchical porosity, PWN/$FeVO_4$@CNF, was fabricated via electrospinning followed by precise calcination. As a LIB anode, this composite demonstrates outstanding performance and significantly enhanced ion/electron transport compared to its individual components. It achieves a high initial discharge capacity of 1327.7 $mA{\cdot}h{\cdot}g^{-1}$ at 0.1 $A{\cdot}g^{-1}$, maintains 1280.0 $mA{\cdot}h{\cdot}g^{-1}$ after 500 cycles, and retains 715.4 $mA{\cdot}h{\cdot}g^{-1}$ even at a rate of 2 $A{\cdot}g^{-1}$. These impressive characteristics derive from its high Li^+ diffusion coefficient, low impedance (R_s, R_{ct}, and Z_w), and a large electrochemically active surface area. Kinetic analysis indicates a dual charge storage mechanism, combining diffusion-controlled battery-type behavior ($i \propto v^{1/2}$) and surface-driven pseudocapacitive contributions ($i \propto v$), with the latter becoming increasingly dominant at higher scan rates. Outperforming most reported anode materials, PWN/$FeVO_4$@CNF benefits from a well-designed

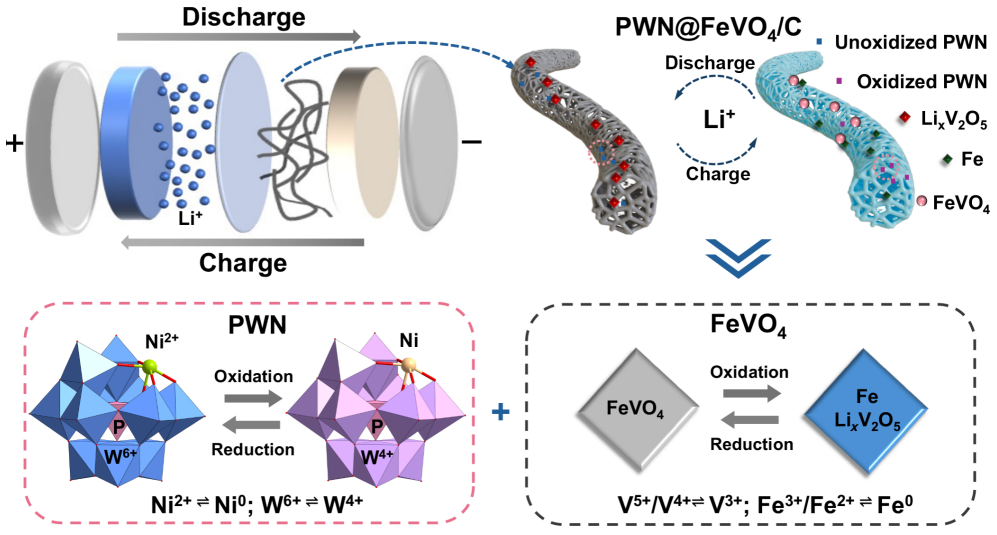

Figure 6 Structure–performance relationship of PWN/$FeVO_4$@CNF composite for enhanced lithium-ion battery applications.

architecture and multicomponent synergy: PWN provides multielectron redox centers and rapid charge transfer, whereas $FeVO_4$ offers a high theoretical capacity and cooperative electronic modulation. The conductive, hierarchically porous nanofiber network further shortens ion/electron pathways and mitigates volume expansion, effectively suppressing the capacity fade common in conventional anodes. This work demonstrates an effective strategy for the homogeneous integration of complementary active phases into 1D hierarchical scaffolds, thereby offering a scalable approach for creating high-performance electrodes for next-generation energy storage devices.

Electronic Supplementary Material: Supplementary material (materials and methods, characterization figures, electrochemical performance diagram, and electrochemical property comparison table) is available in the online version of this article at https://doi.org/10.26599/POM.2026.9140135.

Data availability

All data needed to support the conclusions in the paper are presented in the manuscript and the Electronic Supplementary Material. Additional data related to this paper may be requested from the corresponding author upon request.

Acknowledgements

This work was supported by the National Natural Science Foundation of China (Nos. 22171061 and 42371138) and Harbin Normal University Postgraduate Innovation Project (No. HSDSSCX2025-22).

Declaration of competing interest

The authors declare that they have no known competing financial interests or personal relationships that could have appeared to influence the work reported in this paper.

Author contribution statement

Y. Y. L.: Writing – original draft. Y. W. W.: Methodology, data curation. L. S.: Conceptualization, supervision. P. Y. Z.: Formal analysis. L. P. C.: Visualization, validation. Z. Y. H.: Investigation, software. K. Y.: Writing – review, funding acquisition, project administration.

Use of AI statement

None.

References

[1] Wang, R.; Wang, L.; Liu, R.; Li, X. Y.; Wu, Y. Z.; Ran, F. "Fast-charging" anode materials for lithium-ion batteries from perspective of ion diffusion in crystal structure. *ACS Nano* **2024**, *18*, 2611–2648.

[2] Zhang, C. F.; Chou, S. L.; Guo, Z. P.; Dou, S. X. Beyond lithium-ion batteries. *Adv. Funct. Mater.* **2024**, *34*, 2308001.

[3] Liu, K.; Liu, Y. Y.; Lin, D. C.; Pei, A.; Cui, Y. Materials for lithium-ion battery safety. *Sci. Adv.* **2018**, *4*, eaas9820.

[4] Azuaje-Berbecí, B. J.; Ertan, H. B. A model for the prediction of thermal runaway in lithium-ion batteries. *J. Energy Storage.* **2024**, *90*, 111831.

[5] Soltani, N.; Bahrami, A.; Giebeler, L.; Gemming, T.; Mikhailova, D. Progress and challenges in using sustainable carbon anodes in rechargeable metal-ion batteries. *Prog. Energy Combust. Sci.* **2021**, *87*, 100929.

[6] Yuan, S.; Lai, Q. H.; Duan, X.; Wang, Q. Carbon-based materials as anode materials for lithium-ion batteries and lithium-ion capacitors: A review. *J. Energy Storage.* **2023**, *61*, 106716.

[7] Chen, X. Y.; Liu, Q.; Hou, L. J.; Yang, Q.; Zhao, X. H.; Mu, D. B.; Li, L.; Chen, R. J.; Wu, F. Progress in modification of micron silicon-based anode materials for lithium-ion battery. *J. Energy Storage.* **2024**, *93*, 112286.

[8] Xia, D. W.; Gao, H. P.; Li, M. Q.; Gong, F.; Li, M. Transition metal vanadates electrodes in lithium-ion batteries: A holistic review. *Energy Storage Mater.* **2021**, *35*, 169–191.

[9] Zheng, M. B.; Tang, H.; Li, L. L.; Hu, Q.; Zhang, L.; Xue, H. G.; Pang, H. Hierarchically nanostructured transition metal oxides for lithium-ion batteries. *Adv. Sci.* **2018**, *5*, 1700592.

[10] Ata-ur-Rehman; Iftikhar, M.; Latif, S.; Jevtovic, V.; Ashraf, I. M.; El-Zahhar, A. A.; Saleh, E. A. M.; Abbas, S. M. Current advances and prospects in NiO-based lithium-ion battery anodes. *Sustain. Energy Technol. Assess.* **2022**, *53*, 102376.

[11] Ni, L. B.; Gu, J.; Jiang, X. Y.; Xu, H. J.; Wu, Z.; Wu, Y. C.; Liu, Y.; Xie, J.; Wei, Y. G.; Diao, G. W. Polyoxometalate-cyclodextrin-based

cluster-organic supramolecular framework for polysulfide conversion and guest-host recognition in lithium-sulfur batteries. *Angew. Chem., Int. Ed.* **2023**, *62*, e202306528.

[12] Chaluvachar, P.; Sudhakar, Y. N.; Mahesha, G. T.; Nair, V. G.; Pai, D. K. Polyoxometalate-based hybrid supercapacitors: Advances, challenges, and future prospects in sustainable energy storage. *Chem. Eng. J. Adv.* **2025**, *24*, 100908.

[13] Yuan, G. B.; Ge, H. Y.; Shi, W. X.; Liu, J. L.; Zhang, Y.; Wang, X. Hybrid sub-1 nm nanosheets of Co-assembled $MnZnCuO_x$ and polyoxometalate clusters as anodes for Li-ion batteries. *Angew. Chem., Int. Ed.* **2023**, *62*, e202309934.

[14] Liu, J. X.; Zhang, X. B.; Li, Y. L.; Huang, S. L.; Yang, G. Y. Polyoxometalate functionalized architectures. *Coord. Chem. Rev.* **2020**, *414*, 213260.

[15] Hou, Y. S.; Cui, L. P.; Wang, Q.; Wang, M. L.; Li, G.; Yu, K. The ternary composite formed by intercalation of porous Keggin-type POM and lamellar MoS_2 into accordion-like MXene for enhanced electrochemical properties of the LIBs. *Chem. Eng. J.* **2025**, *507*, 160503.

[16] Gautam, J.; Liu, Y.; Gu, J.; Ma, Z. Y.; Dahal, B.; Chishti, A. N.; Ni, L. B.; Diao, G. W.; Wei, Y. G. Three-dimensional nano assembly of nickel cobalt sulphide/polyaniline@polyoxometalate/reduced graphene oxide hybrid with superior lithium storage and electrocatalytic properties for hydrogen evolution reaction. *J. Colloid Interface Sci.* **2022**, *614*, 642–654.

[17] Cui, L. P.; Sun, S.; Yu, K.; Zhang, S.; Wang, M. L.; Chen, J. J.; Zhou, B. B. High-rate lithium-ion battery performance of a ternary sea urchin-shaped $CoNiO_2$@NiP_6Mo_{18}/CNTs composites. *J. Energy Chem.* **2024**, *96*, 516–525.

[18] Ullah, I.; Aldhafeeri, T. R.; Haider, A.; Wu, X. Y.; Ullah, Z.; Chang, S. Y.; Innayat, A.; Begum, N.; Pope, M. A.; Sher, F. et al. Layered arrangement of polyoxometalate on a metal-organic framework as a high-capacity anode material for sodium-ion batteries. *ACS Appl. Energy Mater.* **2025**, *8*, 1743–1751.

[19] Ge, S. H.; Cui, L. P.; Yu, K.; Wang, M. L.; Guo, L. X.; Zhou, B. B. Basket-like POMs and ZnO co-modified CNFs as anode of high-efficient Lithium-ion batteries. *J. Energy Storage.* **2024**, *93*, 112312.

[20] Tang, W. S.; Qiu, T. Y.; Hu, Z. Y.; Li, Y. Q.; Yao, R. Q.; Wang, Y. H.; Lang, X. Y.; Tan, H. Q.; Li, Y. G.; Jiang, Q. Monodisperse manganese-vanadium-oxo clusters with extraordinary Lithium Storage. *Adv. Sci.* **2024**, *11*, 2402616.

[21] Huang, S. C.; Lin, C. C.; Hu, C. W.; Liao, Y. F.; Chen, T. Y.; Chen, H. Y. Vanadium-based polyoxometalate as electron/ion sponge for lithium-ion storage. *J. Power Sources.* **2019**, *435*, 226702.

[22] Tao, B. X.; Li, X. L.; Ye, C.; Zhang, Q.; Deng, Y. H.; Han, L.; Li, L. J.; Luo, H. Q.; Li, N. B. One-step hydrothermal synthesis of cobalt-vanadium based nanocomposites as bifunctional catalysts for overall water splitting. *Nanoscale.* **2019**, *11*, 18238–18245.

[23] Kim, C. S.; Lee, J. S.; Saroha, R.; Park, Y. B.; Kang, Y. C.; Kang, D. W.; Jeong, S. M.; Cho, J. S. Porous nitrogen-doped graphene nanofibers comprising metal organic framework-derived hollow and ultrafine layered double metal oxide nanocrystals as high-performance anodes for lithium-ion batteries. *J. Power Sources.* **2022**, *523*, 231030.

[24] Jia, F. D.; Wang, F. F.; Pan, J. H.; Sun, C. X.; Zhang, R. S.; Jiao, C. X.; Gao, C.; Sang, J. J.; Xu, Y. P.; Wang, Q. Electrospun metal-organic framework materials derived bimetallic oxides as high-efficiency anodes for lithium-ion battery. *J. Alloys Compd.* **2024**, *1006*, 176201.

[25] Lian, Y.; Zheng, Y. J.; Wang, D. W.; Bai, Y. Q.; Yan, H. S.; Wang, Z. F.; Zhao, J.; Zhang, H. H. Ultrafast and stable ion/electron transport of $MnNb_2O_6$ in LIC/SC via interface protection and lattice defects. *J. Colloid Interface Sci.* **2022**, *606*, 77–86.

[26] Pullanchiyodan, A.; Joy, R.; Sreeram, P.; Raphael, L. R.; Das, A.; Balakrishnan, N. T. M.; Ahn, J. H.; Vlad, A.; Sreejith, S.; Raghavan, P. Recent advances in electrospun fibers based on transition metal oxides for supercapacitor applications: A review. *Energy Adv.* **2023**, *2*, 922–947.

[27] Zhong, X. W.; Huan, H. J.; Liu, X. W.; Yu, Y. Facile synthesis of porous germanium-iron bimetal oxide nanowires as anode materials for lithium-ion batteries. *Nano Res.* **2018**, *11*, 3702–3709.

[28] Wang, X. L.; Kim, E. M.; Senthamaraikannan, T. G.; Lim, D. H.; Jeong, S. M. Porous hollow high entropy metal oxides $(NiCoCuFeMg)_3O_4$ nanofiber anode for high-performance lithium-ion batteries. *Chem. Eng. J.* **2024**, *484*, 149509.

[29] Shao, S. X.; Liu, B. Y.; Zhang, M.; Yin, J. L.; Gao, Y. Y.; Ye, K.; Yan, J.; Wang, G. L.; Zhu, K.; Cao, D. X. Synthesis and electrochemical performance of $LiVO_3$ anode materials for full vanadium-based lithium-ion batteries. *J. Energy Storage.* **2021**, *35*, 102254.

[30] Kim, H. S.; Nam, K. H.; Park, C. M. Monoclinic vanadium diphosphide as a high-performance lithium-ion battery anode. *J. Alloys Compd.* **2021**, *875*, 160061.

[31] Yang, J.; Li, L. Q.; Zhang, Y.; Zhang, Y. F.; Sun, C. C.; Tan, H. T.; Huang, W.; Yan, Q. Y.; Dong, X. C. Vanadium carbide based composite for high performance oxygen reduction reaction and lithium ion batteries. *ChemistrySelect.* **2016**, *1*, 2682–2686.

[32] Park, E.; So, S.; Hur, J. Carbon-free hydrated cobalt vanadium oxide as a promising anode for lithium-ion batteries. *Appl. Surf. Sci.* **2022**, *579*, 152182.

[33] Wu, Y. S.; Zhan, L.; Huang, K. T.; Wang, H. J.; Yu, H.; Wang, S. Q.; Peng, F.; Lai, C. Y. Iron based dual-metal oxides on graphene for lithium-ion batteries anode: Effects of composition and morphology. *J. Alloys Compd.* **2016**, *684*, 47–54.

[34] Abdah, M. A. A. M.; Azman, N. H. N.; Kulandaivalu, S.; Sulaiman, Y. Review of the use of transition-metal-oxide and conducting polymer-based fibres for high-performance supercapacitors. *Mater. Des.* **2020**, *186*, 108199.

[35] Coronel, N. C.; da Silva, M. J.; Ferreira, S. O.; da Silva, R. C.; Natalino, R. K5PW11NiO39-catalyzed oxidation of benzyl alcohol with hydrogen peroxide. *ChemistrySelect.* **2019**, *4*, 302–310.

[36] Ensafi, A. A.; Heydari-Soureshjani, E.; Jafari-Asl, M.; Rezaei, B. Polyoxometalate-decorated graphene nanosheets and carbon nanotubes, powerful electrocatalysts for hydrogen evolution reaction. *Carbon.* **2016**, *99*, 398–406.

[37] Liu, Z. D.; Lu, Q. F.; Wei, M. Z.; Guo, E. Y. $FeVO_4$ nanobelts: Controllable synthesis by electrospinning and visible-light photocatalytic properties. *J. Sol-Gel Sci. Technol.* **2017**, *82*, 67–74.

[38] Ghani, F.; An, K.; Lee, D. Effect of calcination temperature on the physicochemical properties and electrochemical performance of $FeVO_4$ as an anode for lithium-ion batteries. *Materials.* **2023**, *16*, 565.

[39] Biesinger, M. C.; Payne, B. P.; Grosvenor, A. P.; Lau, L. W. M.; Gerson, A. R.; Smart, R. S. C. Resolving surface chemical states in XPS analysis of first row transition metals, oxides and hydroxides: Cr, Mn, Fe, Co and Ni. *Appl. Surf. Sci.* **2011**, *257*, 2717–2730.

[40] Bagus, P. S.; Nelin, C. J.; Brundle, C. R.; Crist, B. V.; Ilton, E. S.; Lahiri, N.; Rosso, K. M. Main and satellite features in the Ni 2p XPS of NiO. *Inorg. Chem.* **2022**, *61*, 18077–18094.

[41] Payne, B. P.; Biesinger, M. C.; McIntyre, N. S. The study of polycrystalline nickel metal oxidation by water vapour. *J. Electron Spectrosc. Relat. Phenom.* **2009**, *175*, 55–65.

[42] Grosvenor, A. P.; Biesinger, M. C.; Smart, R. S. C.; McIntyre, N. S. New interpretations of XPS spectra of nickel metal and oxides. *Surf. Sci.* **2006**, *600*, 1771–1779.

[43] Ji, T.; Chen, W. L.; Kang, Z. H.; Zhang, L. M. Polyoxometalates for continuous power generation by atmospheric humidity. *Nano Res.* **2024**, *17*, 1875–1885.

[44] Ding, Y. H.; Peng, J.; Khan, S. U.; Yuan, Y. A new polyoxometalate (POM)-based composite: Fabrication through POM-assisted

polymerization of dopamine and properties as anode materials for high-performance lithium-ion batteries. *Chem.—Eur. J.* **2017**, *23*, 10338–10343.
[45] Eshaq, G.; Wang, S. B.; Sun, H. Q.; Sillanpaa, M. Superior performance of $FeVO_4$@CeO_2 uniform core-shell nanostructures in heterogeneous Fenton-sonophotocatalytic degradation of 4-nitrophenol. *J. Hazard. Mater.* **2020**, *382*, 121059.
[46] Li, J. H.; Zhao, W.; Guo, Y.; Wei, Z. B.; Han, M. S.; He, H.; Yang, S. G.; Sun, C. Facile synthesis and high activity of novel $BiVO_4$/$FeVO_4$ heterojunction photocatalyst for degradation of metronidazole. *Appl. Surf. Sci.* **2015**, *351*, 270–279.
[47] Wang, L.; Wang, J. B.; Cheng, H. P.; Zhou, X. X.; Ma, Z. $Ce_{1-x}Fe_xVO_4$ with improved activity for catalytic reduction of NO with NH_3. *Catalysts.* **2022**, *12*, 549.
[48] Sim, D. H.; Rui, X. H.; Chen, J.; Tan, H. T.; Lim, T. M.; Yazami, R.; Hng, H. H.; Yan, Q. Y. Direct growth of $FeVO_4$ nanosheet arrays on stainless steel foil as high-performance binder-free Li ion battery anode. *RSC Adv.* **2012**, *2*, 3630–3633.
[49] Zhu, P. P.; Sheng, N.; Li, M. T.; Li, J. S.; Liu, G. D.; Yang, X. Y.; Sha, J. Q.; Zhu, M. L.; Jiang, J. Z. Fabrication and electrochemical performance of unprecedented POM-based metal-carbene frameworks. *J. Mater. Chem. A* **2017**, *5*, 17920–17925.
[50] Huang, Q.; Wei, T.; Zhang, M.; Dong, L. Z.; Zhang, A. M.; Li, S. L.; Liu, W. J.; Liu, J.; Lan, Y. Q. A highly stable polyoxometalate-based metal-organic framework with π-π stacking for enhancing lithium ion battery performance. *J. Mater. Chem. A* **2017**, *5*, 8477–8483.
[51] Ghani, F.; Raza, A.; Kyung, D.; Kim, H. S.; Lim, J. C.; Nah, I. W. Optimization of synthesis conditions of high-tap density $FeVO_4$ hollow microspheres via spray pyrolysis for lithium-ion batteries. *Appl. Surf. Sci.* **2019**, *497*, 143718.
[52] Liu, X. L.; Cao, Y. C.; Zheng, H.; Chen, X.; Feng, C. Q. Synthesis and modification of $FeVO_4$ as novel anode for lithium-ion batteries. *Appl. Surf. Sci.* **2017**, *394*, 183–189.
[53] Brezesinski, T.; Wang, J.; Tolbert, S. H.; Dunn, B. Ordered mesoporous α-MoO_3 with iso-oriented nanocrystalline walls for thin-film pseudocapacitors. *Nat. Mater.* **2010**, *9*, 146–151.
[54] Augustyn, V.; Simon, P.; Dunn, B. Pseudocapacitive oxide materials for high-rate electrochemical energy storage. *Energy Environ. Sci.* **2014**, *7*, 1597–1614.
[55] Shi, L.; Liu, W.; Zhao, F. J.; Liu, R. X.; Sun, Y. D.; Dong, C. Y.; Cheng, G. G.; Ding, J. N. Tailoring the dual precursors coupled hard carbon by embedding the pitch-derived graphitic domains to achieve high-performance sodium storage. *J. Power Sources.* **2024**, *596*, 234093.
[56] Yin, X. X.; Wu, D. H.; Lu, Z. J.; Xie, J.; Hu, J. D.; Tang, M. X.; Ma, H.; Zhang, X. T.; Cao, Y. L. Innovative synthesis and comprehensive electrochemical evaluation of $FeVO_4$ for enhanced sodium-ion battery performance. *Appl. Energy.* **2024**, *373*, 123872.
[57] Li, Y. L.; Fan, Z. Q.; Peng, Z. J.; Xu, Z. H.; Zhang, X. Y.; Zhou, J. E.; Lin, X. M.; Wu, Z. Y.; Zhao, E. Y.; Zeng, R. H. Metal-organic framework-derived $LiFePO_4$/C composites for lithium storage: *In situ* construction, effective exploitation, and targeted restoration. *EcoMat.* **2023**, *5*, e12415.
[58] Meng, L. C.; Guo, R. S.; Peng, J. H.; An, L. Y.; Zhao, S. Q. Facile synthesis of hairbrush like $FeVO_4$@C/CC anode material with enhanced electrochemical performance for alkaline ion batteries. *J. Appl. Electrochem.* **2023**, *53*, 991–1002.
[59] Yang, J.; Tan, R.; Li, D.; Ma, J. M.; Duan, X. C. Ionic liquid assisted electrospinning of porous $LiFe_{0.4}Mn_{0.6}PO_4$/CNFs as free-standing cathodes with a pseudocapacitive contribution for high-performance lithium-ion batteries. *Chem.—Eur. J.* **2020**, *26*, 5341–5346.
[60] Lan, B. X.; Tang, C.; Chen, L. N.; Zhang, W. W.; Tang, W.; Zuo, C. L.; Fu, X. D.; Dong, S. J.; An, Q. Y.; Luo, P. $FeVO_4 \cdot nH_2O$@rGO nanocomposite as high performance cathode materials for aqueous Zn-ion batteries. *J. Alloys Compd.* **2020**, *818*, 153372.

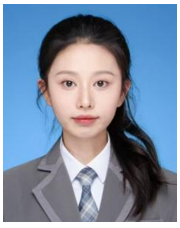

Yangyang Liu her B.S. degree in chemistry (normal) from Harbin Normal University in 2022. She is currently studying for a master's degree in inorganic chemistry in Prof. Kai Yu's group in Harbin Normal University. Her research interest is the preparation of polymetallic oxide salt anode material.

Yuwen Wang was awarded her Bachelor of Science degree in Chemistry (Teacher Training) from Harbin Normal University in 2020. She is currently a doctoral candidate in Biochemistry and Molecular Biology under the guidance of Professor Kai Yu at Harbin Normal University. Her research interests cover the fabrication of polyoxometalate-based solid electrolytes and electrocatalysts, as well as the biochemical properties of polyoxometalates.

Li Sun received the B.Sc., M.Sc. and Ph.D. degrees in Physical Geography at Harbin Normal University, Harbin, Heilongjiang Province, China, in 2006, 2010 and 2014, respectively. She is currently an Assistant Professor and Doctoral Supervisor with the School of Geographical Sciences, Harbin Normal University. She teaches soil geography at the undergraduate level and English at Ph.D. level. Her main research interests include the application of geographic information system in the Field of Environmental Science.

Pengyu Zhu is an undergraduate student at the School of Chemistry and Chemical Engineering, Harbin Normal University, enrolled in 2024 and joined Professor Yu Kai's research group in 2025. His research focuses on the design, synthesis, and electrochemical properties of polyoxometalates.

Liping Cui is an associate professor and master's thesis advisor at Harbin Normal University. She earned her Ph.D. through a combined master's-to-Ph.D. program under the supervision of Prof. Kai Yu from 2017 to 2022. She subsequently conducted postdoctoral research in Prof. Jiajia Chen's laboratory at Xiamen University and began her academic career in 2025 upon completing her postdoctoral fellowship. Her research primarily focuses on the synthesis, design, and functional assembly of polymetallic oxygen clusters, as well as their fundamental applications in the field of energy conversion and storage.

Han Ziyue earned a Bachelor of Science degree in Chemistry (normal) from Harbin Normal University in 2020. She is currently pursuing a Master of Science degree in Inorganic Chemistry under the supervision of Professor Yu Kai at Harbin Normal University. Her research focuses on lithium-sulfur battery cathodes modified with polyoxometalates.

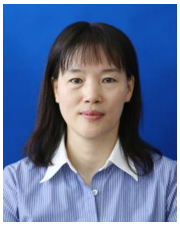

Yu Kai is a professor and doctoral supervisor at Harbin Normal University. She received her Ph.D. from School of Chemical Engineering and Chemistry, Harbin Institute of Technology in 2012. Her research work mainly focuses on the design and synthesis of functional polyoxometalate materials and their applications in the fields of catalysis, pharmaceuticals and energy storage.